Nanoscale

Accepted Manuscript

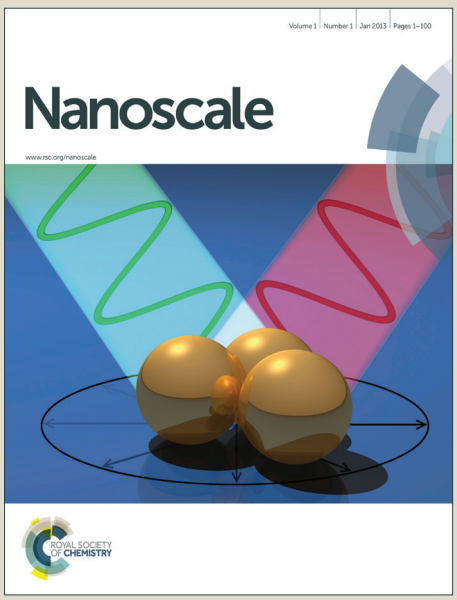

ROYAL SOCIETY OF CHEMISTRY

www.rsc.org/nanoscale

Journal Name

ARTICLE

Tailoring chiro-optical effects by helical nanowire arrangement

Marco Esposito, [a,b] Vittorianna Tasco,* [a] Francesco Todisco, [a] Alessio Benedetti, [c] Iolena Tarantini, [b] Massimo Cuscunà, [a] Lorenzo Dominici, [a] Milena De Giorgi [a] and Adriana Passaseo [a]

Received 00th January 20xx,
Accepted 00th January 20xx

DOI: 10.1039/x0xx00000x

www.rsc.org/

In this work, we experimentally investigate the chiro-optical properties of 3D metallic helical systems at optical frequencies. Both single and triple-nanowires geometries have been studied. In particular, we found that in single-helical nanostructures, the enhancement of chiro-optical effects achievable by geometrical design is limited, especially with respect to the operation wavelengths and to the circular polarization conversion purity. Conversely, in triple-helical nanowire configuration, the dominant interaction is the coupling among intertwined coaxial helices which is driven by a symmetric spatial arrangement. Consequently, a general improvement in g-factor, extinction ratio and signal-to-noise-ratio is achieved in a broad spectral range. Moreover, while in single-helical nanowires a mixed linear and circular birefringence results in an optical activity strongly dependent on sample orientation and wavelength, in triple-helical nanowire configuration, the obtained purely circular birefringence leads to a large optical activity up to 8°, independent on the sample angle, and standing in a broad band of 500 nm in the visible range. These results demonstrate a strong correlation between the configurational internal interactions and the chiral feature designation, which can be effectively exploited for nanoscale chiral device engineering.

1. Introduction

In the recent years, there has been growing interest in the chiral nanophotonics field where advanced photonic devices can be engineered [1-2] in order to tailor exciting chiro-optical properties that in the natural world are normally faint or not existing at all, such as negative refraction [3]. In particular, chiral plasmonic nanostructures have already shown exotic properties, such as enhanced chiral sensing [4] and polarization control [5-8]. Since chirality has its highest expression in 3D objects, a large number of quasi-three-dimensional geometries and arrangements have been proposed [9-16]. Among them, the helical structural configuration was appraised as the ideal structure to manifest maximized chiral response in the far field.

Indeed, helix-shaped metamaterials by Direct Laser Writing (DLW) [2,17] have been suggested as compact and broadband circular polarizers or polarization converter [18] in the IR range, while, most recently, focused ion and electron beam induced deposition (FIBID/FEBID) technologies have enabled the nanoscaling of fully 3D helical metamaterials to operate in the near infrared to visible range [19, 20].

However, the experimental optical results presented so far on single helical nanowire (SHN) structures, have expressed great skill to control the circular dichroism, but have shown poor values for other important chiral parameters, required for advanced photonic devices, such as extinction ratio (ER), purity of the transmitted polarized light (low signal-to-noise ratio (SNR)) [21] and optical activity. In order to overcome these drawbacks, 3D complex intertwined multi helical nanowire (MHN), packed in a single unit cell, were theoretically [21-24] proposed and recently realized by Tomographic Rotatory Growth (TRG) method [25].

In this work, we experimentally compare the chiro-optical properties of metallic helical systems with different structural arrangements at the nanoscale. We found that the circular dichroism, the ER and the SNR values achievable in SHN structures are limited by the intrinsic structural configuration. Geometrical parameter variations, as shown for a closely packed SHN arrangement, can enhance some chiral properties, but these effects exist for narrow frequency intervals, as well as the intensity and the SNR of light transmitted through the arrays are worsened. On the other hand, the interaction between the individual intertwined helical nanowires arranged in a 3-fold symmetry, as in triple helical nanowires (THNs), is effective not only in increasing the g factor up to 70% and doubling the ER with respect to SHNs, but also in improving the SNR up to 25 dB. Moreover, we found that, differently

[a] CNR NANOTEC - Istituto di Nanotecnologia, Polo di Nanotecnologia, c/o Campus Ecotekne, via Monteroni 73100 Lecce, Italy. E-mail: vittorianna.tasco@nanotec.cnr.it
[b] Università del Salento Dip. Mat-Fis Ennio De Giorgi, I-73100 Lecce, Italy.
[c] Universita` di Roma La Sapienza, Dip. SBAI, via Scarpa 16, 00161 Roma, Italy.
† Electronic supplementary information (ESI) available: Spectra of the different transmitted light components; g-factor and ORD maps as a function of the lattice period.
See DOI: 10.1039/x0xx00000x

from SHN systems, where linear (LB) and circular (CB) birefringence are mixed as a function of sample orientation and wavelength, the THN arrangement shows an optical rotatory dispersion (ORD) independent on the sample orientation with respect to the incoming linear polarization, in a broad wavelength range (from 800 nm to 1050 nm), as a result of the increased geometric symmetry.

2. Experimental

We used the Carl Zeiss Auriga 40 Crossbeam FIB/SEM system to fabricate helical nanowire structures by Trimethyl(methylcyclopentadienyl)-platinum(IV) precursor on ITO/glass substrate. The chamber pressure ranged from $1x10^{-5}$ to $8x10^{-6}$ mbar during the deposition process and a refresh time, among single helical structures, together with dose compensation method are employed to recover the pressure drop due to the local depletion of the material density. The growth of THNs was obtained by employing the Tomographic Rotatory Growth method [25]. The helical nanostructure arrays were grown with ion beam current of 1 pA, accelerating voltage of 30 keV and step size of 10 nm.

The circular dichroism and ER spectra of fabricated arrays were obtained by optical confocal transmission setup with a x10 objective lens (numerical aperture 0.45) under normally incident light of a halogen lamp. The circular polarization of incident light was achieved using a combination of a linear polarizer and an achromatic quarter-wave plate. The circular polarization conversion was measured by placing a second pair of linear polarizer and achromatic quarter-wave plate along the detection path. The SNR was calculated as in ref.16. A linearly polarized incident light was used to measure the ORD and the transmitted light was analyzed by a combination of an achromatic half-plate and a linear polarizer. The samples were rotated around their normal axis in step of 30° and the ORD for each angle was performed rotating the half-plate in step of 2°.

The optical responses in the visible range of SHN, CP-SHN and THN arrays were calculated by Lumerical FDTD Solutions employing the Maxwell-Garnett approach to evaluate the material permittivity of the platinum-carbon alloy [20]. The substrate has not been included in the simulations.

3. Results and Discussion

Fig. 1 shows the helical metamaterial arrays, fabricated by FIBID using $(CH_3)_3(CH_3C_5H_4)Pt$ precursor, following the growth procedure in [20] and the TRG method [25], respectively, where the dose compensation technique [19] was employed ian order to suppress the 3D proximity effects. The SHNs in Fig. 1b have 1 loop, external diameter (ED) = 380 nm, wire diameter (WD) = 110 nm, vertical pitch (VP) = 705 nm. The 3-fold configuration of THNs (Fig. 1c) is obtained by three bundled SHNs arranged every 120°, each one with the same shape and dimensions of the SHN in Fig. 1b. The vertical spacing (sub-VP) between two adjacent helical wires is 235 nm, as shown in Fig. 1a. Both the arrays have square lattice with period (LP) of 900 nm. Finally, Fig. 1d shows a closely packed SHN sample (CP-SHN) consisting of a more compact configuration with VP and LP shrunk down to 300 nm and 700 nm, respectively, and increased loop number (n=3). All samples were fabricated on glass substrates covered by ITO.

In order to characterize the chiral helical based arrays, we performed normal incidence transmittance spectra of right (T_{RCP})- and left (T_{LCP})- handed circularly polarized light to rate the dissymmetry factor ($g = 2(T_{LCP} - T_{RCP})/(T_{LCP} + T_{RCP})$) and the extinction ratio ($ER = T_{LCP}/T_{RCP}$).

For the specific geometry of SHN (Fig. 1b), we observe a nearly null circular dichroism and ER constantly equal to 1 in the visible range. A more compact and closely packed geometry like the one of the CP-SHN (Fig. 1d) results effective in inducing a pronounced circular polarization sensitivity between 500 nm and 800 nm, with a maximum g factor of 25%, as an effect of increased loop number and light matter interaction volume. In both these single helical nanowire samples the crossing point between the circularly polarized transmission curves is at 800 nm.

However, if we analyze the behavior of the intertwined arrangement of THN (Fig. 1c), a more effective enhancement in circular dichroism selectivity and bandwidth is evident, with a g factor up to 70% and an ER reaching 2.2, as shown in Fig. 2a-b. This configurational dependence of the chiral features is also analyzed and confirmed by numerical simulations performed by using a Finite Difference Time Domain-based commercial software (Lumerical) and shown in Fig. 2c-d. The simulated spectra show a good agreement for SHN and THN arrays while in the numerical simulation of the CP-SHN array the agreement is only qualitative. As described in ref. 20, the transmission values (and, consequently, the g-factors) strongly depend from the wire metal content that, in turn, is related to the deposition parameters. While in the SHN and THN, the structure exposure time to the ion beam energy is limited to the growth of a single loop, in the CP-SHN, the higher loop number requires longer exposure. Therefore, the 3D proximity effects affecting the growth are enhanced, thus modifying the Pt content and its distribution along the wire [26-27]. As a consequence, the permittivity of the platinum-carbon alloy used for the numerical simulations, evaluated by the Maxwell-Garnett approach describes with a good approximation the SHN and THN array behavior. On the other hand, a more precise quantitative description of the CP-SHN response could be obtained by developing a more complex wire structural model, induced by cumulative 3D proximity effects. Additional information on circularly polarized light interaction with these structures and on their possible implementation as miniaturized and high purity circular polarizers are provided by the SNR spectra obtained from the transmission curves and the polarization conversion measurements (Fig. S1†). As shown in Fig. 3, both the single nanowire arrays under investigation show poor SNR, lower than 10 dB. Most noticeably, the CP-SHN arrangement exhibits a reduced SNR

with respect to the SHN sample in the long wavelength region. On the other hand, the THN array exhibits a SNR > 10 dB over the entire visible range, with a maximum value of 25 dB between 500 and 600 nm, suggesting that LCP and RCP are the eigenpolarizations of our THN structures throughout the measured spectral region. The general improvement of chiral performances in the THNs with respect to the SHNs can be inferred to the mutual interaction between excited surface plasmon modes between the individual intertwined helical nanowires. In particular, this interaction is responsible of the widening of the dichroic band covering all the visible range with respect to the SHN case (bandwidth of 200 nm) and the CP-SHN case (bandwidth of 300 nm). On the other hand, the purity of the transmitted circularly polarized light (expressed by the SNR parameter) is a property dependent on the circularity of the light-induced current path within the helix-based system [22]. In the general SHN case, the interaction between excited surface plasmon modes occurs above all between neighboring helices (external coupling). The loose arrangement of SHN sample (Fig. 1b), where the LP is >> ED, allows to strongly reduce such external interactions and to increase the average amount of transmitted light. However, as shown in Fig. 3, a maximum SNR value of 10 dB is reached at the expense of the circular dichroism and the ER. Geometrical parameters actually provide an effective means to engineer chiro-optical properties [20]. This is demonstrated by the large g-factor increment in CP-SHN sample, accompanied by an improvement in ER and bandwidth, basically induced by the large filling factor per volume. However, as a drawback, this denser and more closely packed arrangement transmits, in average, a lower light intensity, which is undesirable for devices applications.

Journal Name

ARTICLE

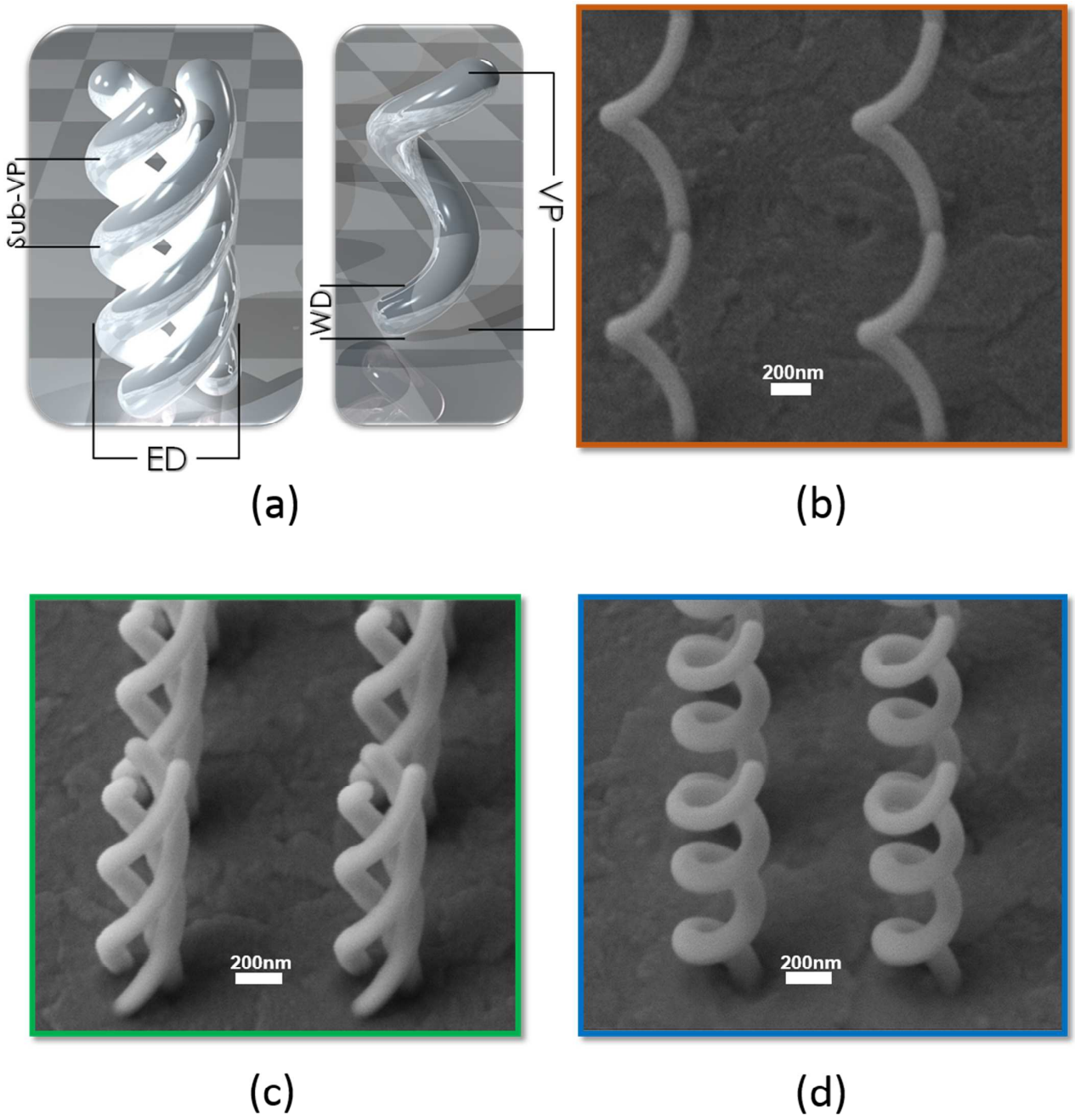

Fig. 1. (a) Schematic representation of SHN and THN geometrical parameters. Scanning electron microscope zoomed views of SHN (b), THN (c) and CP-SHN (d) arrays grown by FIBID of platinum on ITO/glass substrate. In all samples, WD and ED are kept constant at 110 nm and 380 nm, respectively.

Journal Name

ARTICLE

Moreover, the close planar arrangement boosts the mutual helix interaction and leads to a lower purity of circularly polarized transmitted signals, as evident by the lower SNR (Fig. 3). Conversely, in THNs, even if the intertwined helical nanowires are characterized by strong internal coupling, the spatially symmetric arrangement leaves unaffected the current path and strongly reduces the contribution of the opposite polarization, thus resulting in a higher SNR (up to 25 dB), as shown in Fig. 3. Therefore, a higher SNR can be achieved, despite LP >> ED, because of the 3-fold symmetry arrangement.

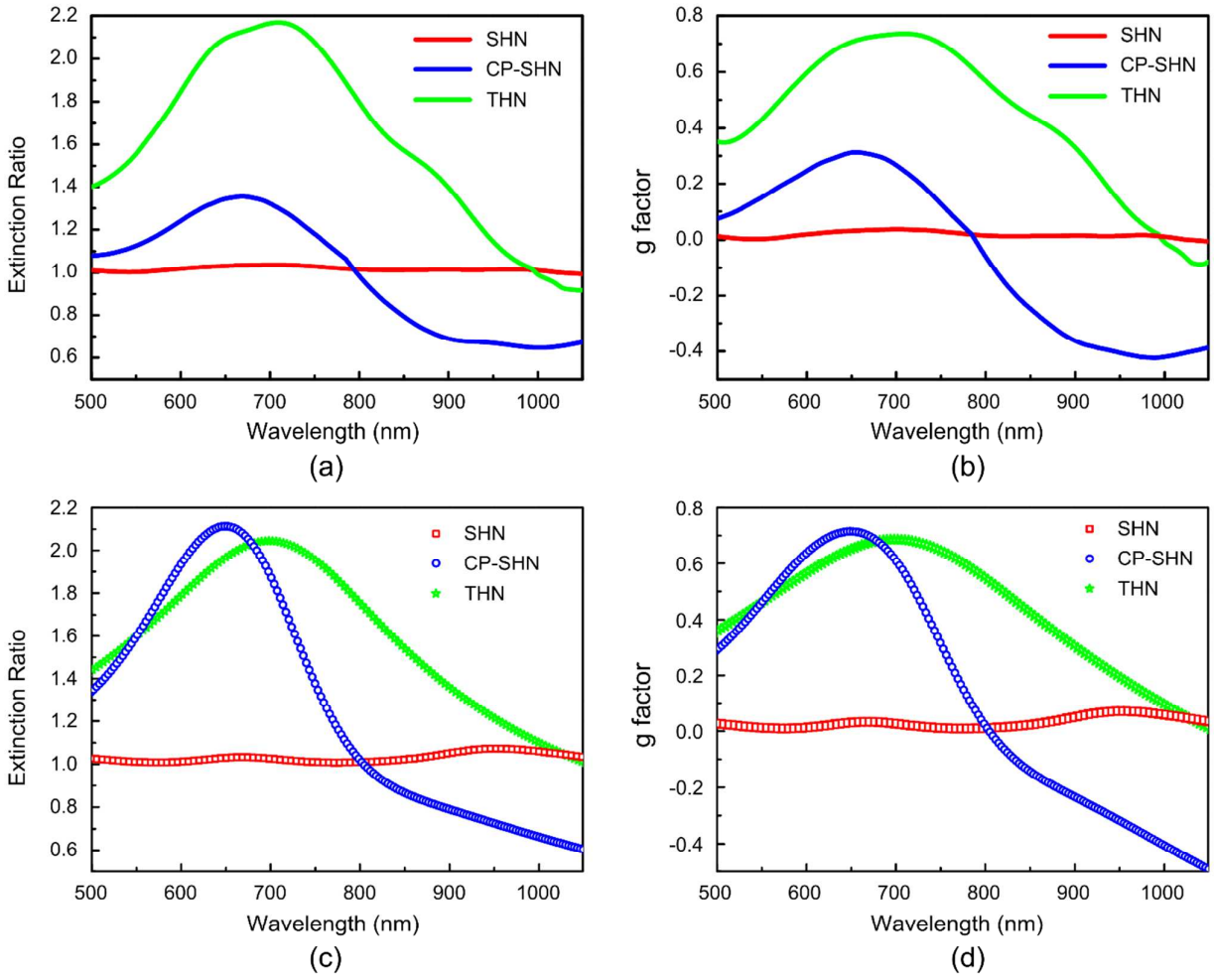

Fig. 2. Measured ER, defined as = T_{LCP}/T_{RCP} (a), and g factor (b) spectra for SHN (red line), CP-SHN (blue line) and THN (green line) arrays in the optical frequency region. The lower panel shows the same parameters (extinction ratio (c) and g factor (d)) as simulated by FDTD tools, exhibiting a good agreement with experimental data.

Furthermore, the symmetric interaction in THNs results in a stronger circular dichroism (g factor up to 70%) with respect to the SHNs with the same geometrical design (6%) and to the CP-SHNs case (40%), still preserving a high transmittance (~50%). In addition to the circular dichroism, in helix-shaped chiral metamaterials electric and magnetic dipoles can be excited collinearly along the structure vertical axis, giving rise to optical rotation, related to the different refractive index for right (n_{RCP}) and left (n_{LCP}) circular

polarization. In order to investigate the optical activity, we performed optical rotatory dispersion analysis (ORD) over all the SHN, CP-SHN and THN arrays, using linearly polarized incident light. It should be noted that in helical metamaterials, the tip together with the helix axis determines a preferred direction in space that breaks the rotational symmetry, thus introducing intrinsic linear birefringence [21]. Therefore, in order to identify the contribution of the linear birefringence and isolate the true optical activity, as related to the difference in the effective refractive index for the two circularly polarized components, we first measured polarization rotation of the incident linearly polarized light, as a function of the sample angle, for the three sample types (figure 4a-c). Then, we analyzed the polarization rotation angle dependence on the sample orientation at the crossing point, corresponding to the wavelength with null dichroism, and where a pure linear polarization rotation is expected (figure 4d). In these plots, the mean ORD value is the pure optical activity due to only the circular birefringence [6,9] while the modulation with respect to this value arises from the linear birefringence that reveals the impact of the helix anisotropy. In Fig. 4a, we show the measured ORD map for SHN array that exhibits a polarization rotation up to 1.4°, between 30°-60° as azimuth angle of the sample. This low value is an effect of the large lattice period (900 nm) exploited to suppress the external coupling. As expected, the different geometrical arrangement in CP-SHNs leads to a higher optical activity up to 15°, but limited to a narrow frequency region (between 700 and 800 nm) and sample orientation (in the range 60°-120°, Fig. 4b). More quantitatively, by analyzing the ORD maps at the crossing point of the transmittance curves (Fig. 4d), we found a sinusoidal maximum modulation ascribed to the linear birefringence of 0.8°, with a mean value of less than 1° (induced by the CB). Such an ORD modulation is significantly accentuated in the CP-SHN sample that shows an excursion up to 8° around a mean ORD value of 7°. A completely different trend is detected in the THNs, which achieve a strong and very uniform polarization rotation with respect to the sample orientation (Fig. 4c). In this case, at the crossing point (λ = 980 nm) of the two transmission curves, the THNs show 8° of pure optical rotation, constant in the broad wavelength range from 800 nm to 1050 nm with only a faint modulation of < 0.5° versus the azimuthal angle, providing a quantification of the residual anisotropy (extremely weak linear birefringence) related to fabrication tolerances. This effect is related to the recovered rotational symmetry in the 3-fold symmetry arrangement and to the enhanced internal interaction among intertwined helices that prevails on external couplings and boosts the circular birefringence. The strong independence of ORD on sample orientation confirms the critical role of coupling interactions in the helical systems, as driven by the spatial arrangement and symmetry in the multi helical configuration.

In order to better highlight the role of external coupling effects discussed above, we performed FDTD numerical calculations of the electro-magnetic field as a function of the planar inter-helix distance (LP). In particular, for the three sets of samples discussed in this work, we evaluated the spectra of ORD modulation (ΔORD, defined as ORD – ORDavg where ORDavg is the averaged ORD value on the sample orientation for each wavelength), providing direct evaluation of the overall linear birefringence contribution. It is worth noting that the total linear birefringence is induced by the structure intrinsic anisotropy (which in turn is not dependent on the LP parameter) and by the LP-dependent helix mutual interaction, which further adds to the overall system anisotropy. The ΔORD spectra for LP ranging from 500 nm to 1000 nm by steps of 100 nm, are shown in figure 5a-c, while in the supplementary information section the related g-factor and ORD maps are also shown. In the single wire samples (fig. 5a-b) by reducing LP (and consequently, promoting external interactions), ΔORD values increase of nearly one order of magnitude. Conversely, in the THN sample, the linear birefringence component increase with LP is limited (from 0.2° at LP=1000 nm, to 1° at LP=500nm), leading to a predominance of circular birefringence even in very compact arrays, thus suggesting that the interaction of the intertwined helices prevails on the external coupling.

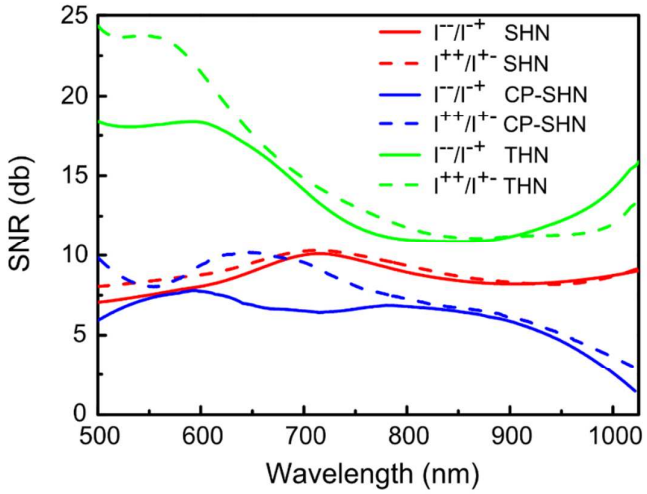

Fig. 3. Measured SNR for SHN (red lines), CP-SHN (blue lines) and THN (green lines) arrays. The SNR for both the incident circular polarizations is calculated as the logarithm of the ratio between the different components of transmitted light, I^{++}, I^{+-} and I^{--}, I^{-+}, where + refers to LCP and - to RCP light. The first index identifies the incident circular polarization while the second index corresponds to the detected polarization components.

Journal Name

ARTICLE

4. Conclusion

In conclusion, we have extensively studied the chiro-optical properties in helical shaped metamaterials with respect to spatial arrangement. In particular, for such a study, we exploited three representative samples where geometrical and structural parameters were chosen in order to identify the role of external coupling among neighbor helices and internal coupling among coaxial intertwined helices. In a loose arrangement with LP >> ED, where the external coupling between neighbor helices is limited, we get poor g factor and ER values, along with modest SNR. A more closely-packed and compact arrangement allows enhancing the chiro-optical properties, with an increment of the g factor (up to 40%) and of the ER, even if in a limited frequency region. However, the external coupling between neighbor helices induces asymmetric interactions, negatively affecting the purity of the transmitted circular polarization. As a consequence, the SNR is worsened and the light transmission degree decreases due to the increased filling factor per volume. On the other hand, the structure engineering by intertwined multiple helix nanowires as in THN system, promotes the internal coupling among coaxial helical nanowires driven by a symmetric spatial configuration. This results beneficial for a large selection of chiro-optical features: a giant g factor (up to 70 %) in a broad dichroic band (extending over 500 nm) and doubled extinction ratio as compared to the CP-SHN case are obtained, along with a higher SNR up to 25 db. The interplay between internal and external coupling among nanohelices induced by the structural arrangement is also effective in tailoring the optical activity of these metamaterials. In the case of single-helical nanowires, a mixed linear and circular birefringence results in an optical activity strongly dependent on sample orientation and wavelength. Conversely, in triple-helical nanowire configuration, the obtained purely circular birefringence leads to an optical activity up to 8°, independent on sample angle, and extending in a broad band of 500 nm in the visible range. These results demonstrate a strong correlation between the internal and external configurational interactions and the chiral property designation, which can be exploited to engineer 3D nanoscale devices with specific chiral features, for potential applications in quantum information, nanophotonic circuits, spintronics, enhanced contrast imaging and enantio-detection in medical and biological applications.

Journal Name

ARTICLE

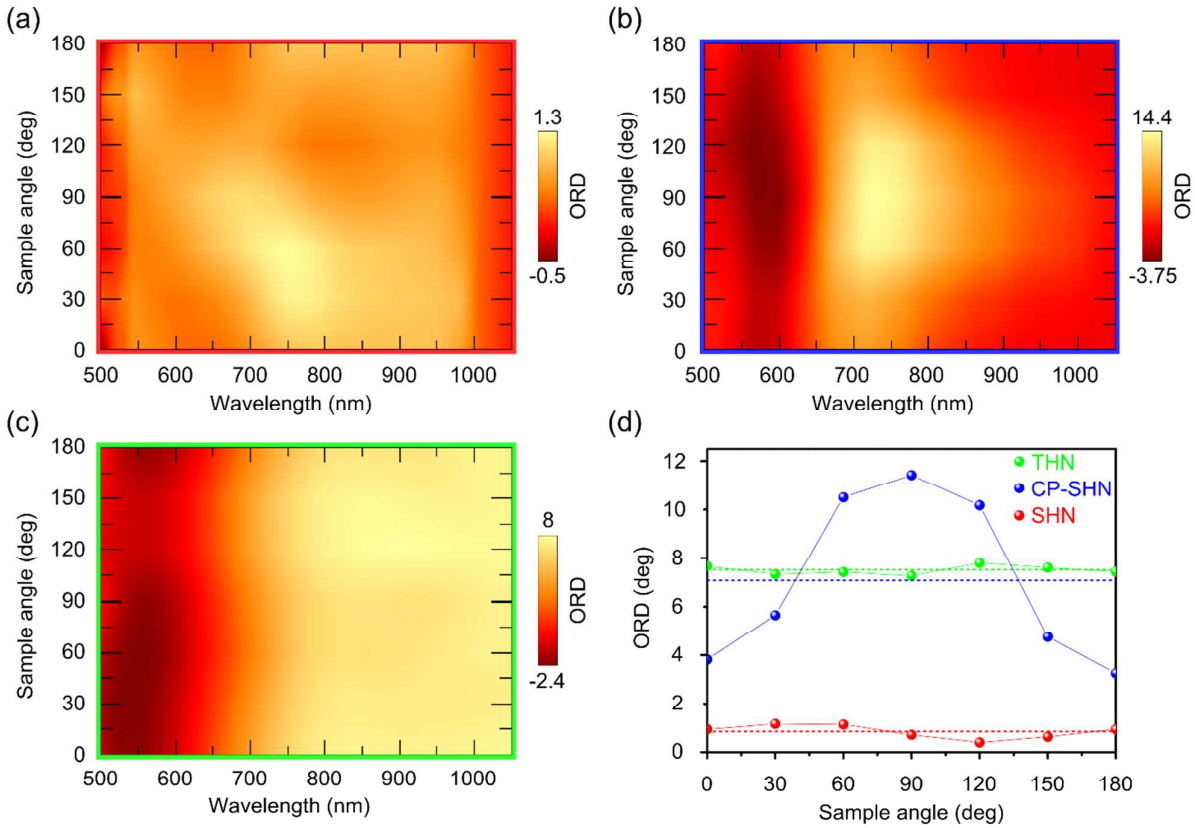

Fig. 4. Measured ORD, at different azimuth angles, of the three analyzed samples: SHN (a), CP-SHN (b) and THN (c). The maxima of the color bars are intentionally different to stand out the ORD behavior and magnitude order in the various helical configurations. (d) Optical activity at the transmission crossing point for SHN, CP-SHN and THN arrays. A very high (faint) modulation due to LB around the mean polarization rotation value due to CB for SHN (THN) array is shown.

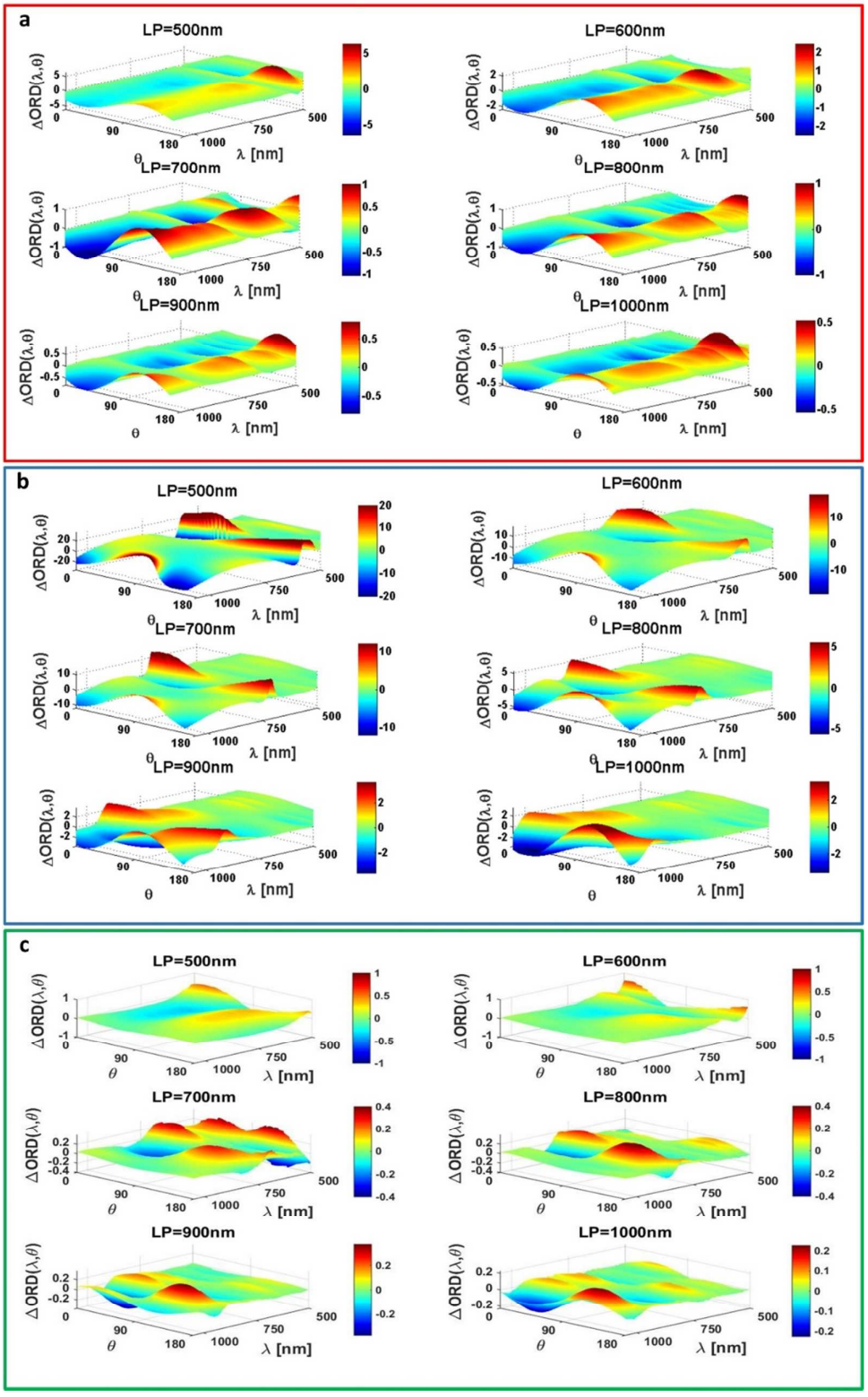

Fig. 5. Numerical simulations of ΔORD (degree) for (a) SHN, (b) CP-SHN and (c) THN as a function of the wavelength (λ) and sample orientation (θ) for each LP value. ΔORD= ORD – ORD_{avg} (where ORD_{avg} is the averaged ORD value on the sample orientation for each wavelength) identifies the modulation, related to the intrinsic anisotropy and external couplings among neighbor helical system (linear birefringence), around the mean value representing the optical activity due to only the circular birefringence.

Journal Name

ARTICLE

Acknowledgments

The work was partially supported by Italian projects PON R&C 2007-2013 "MAAT" Molecular NAnotechnology for HeAlth and EnvironmenT (PON02 00563 3316357). We acknowledge D. Sanvitto for his help in optical spectroscopy and data analysis.

References

1. M. D. Turner, M. Saba, Q. Zhang, B. P. Cumming, G. E. Schröder-Turk and M. Gu. *Nat. Photonics,* 2013, **7**, 801–805.

2. J. K. Gansel, M. Thiel, M. S. Rill, M. Decker, K. Bade, V. Saile, G. von Freymann, S. Linden and M. Wegener, *Science*, 2009, **325**, 1513–1515.

3. J. B. Pendry, *Science*, 2004, **306**, 1353–1355.

4. E. Hendry, T. Carpy, J. Johnston, M. Popland, R. V. Mikhaylovskiy, A. J. Lapthorn, S. M. Kelly, L. D. Barron, N. Gadegaard and M. Kadodwala, *Nat. Nanotechnol.*, 2010, 5, 783-787.

5. M. Decker, M. W. Klein, M. Wegener and S. Linden, *Opt. Lett.*, 2007, **32**, 856–858.

6. M. Kuwata-Gonokami, N. Saito, Y. Ino, M. Kauranen, K. Jefimovs, T. Vallius, J. Turunen and Y. Svirko, *Phys. Rev. Lett.*, 2005, **95**, 227401.

7. K. Konishi, T. Sugimoto, B. Bai, Y. Svirko and K. Kuwata-Gonokami, *Opt. Express*, 2007, **15**, 9575–9583.

8. E. Plum, X. X. Liu, V. A. Fedotov, Y. Chen, D. P. Tsai and N. I. Zheludev, *Phys. Rev. Lett.*, 2009, **102**, 113902 .

9. Y. Cui, L. Kang, S. Lan, S. P. Rodrigues and W. Cai, *Nano Lett.*, 2014, **14**, 1021–1025.

10. M. Decker, M. Ruther, C. E. Kriegler, J. Zhou, C. M. Soukoulis, S. Linden and M. Wegener, *Opt. Lett.*, 2009, **34**, 2501–2503.

11. Y. Zhao, M. A. Belkin and A. Alù, *Nat. Commun.*, 2012, **3**, 870.

12. B. Frank, X. Yin, M. Schäferling, J. Zhao, S. M. Hein, P. V. Braun and H. Giessen, *ACS Nano*, 2013, **7**, 6321–6329.

13. S. P. Rodrigues, S. Lan, L. Kang, Y. Cui and W. Cai, *Adv. Mater.*, 2014, **26**, 6157–6162.

14. M. Hentschel, M. Schäferling, T. Weiss, N. Liu and H. Giessen, *Nano Lett.*, 2012, **12**, 2542–2547.

15. X. Yin, M. Schäferling, B. Metzger and H. Giessen, *Nano Lett.*, 2013, **13**, 6238 −6243.

16. M. Decker, R. Zhao, C. M. Soukoulis, S. Linden and M. Wegener, *Opt. Lett.*, 2010, **35**, 1593–1595.

17. J. K. Gansel, M. Latzel, A. Frolich, J. Kaschke, M. Thiel and M. Wegener, *Appl. Phys. Lett.*, 2012, **100**, 101109.

18. J. Kaschke, L. Blume, L. Wu, M. Thiel, K. Bade, Z. Yang and M. Wegener *Adv. Opt. Mat*. doi: 10.1002/adom.201500194 (2015).

19. M. Esposito, V. Tasco, F. Todisco, A. Benedetti, D. Sanvitto and A. Passaseo, *Adv. Opt. Mat.*, 2014, **2**, 154–161.

20. M. Esposito, V. Tasco, M. Cuscunà, F. Todisco, A. Benedetti, I. Tarantini, M. De Giorgi, D. Sanvitto and A. Passaseo, *ACS Photonics*. 2015, **2**, 105–114.

21. J. Kaschke, J. K. Gansel and M. Wegener, *Opt. Express,* 2012, **20**, 26012–26020.

22. Z. Yang, M. Zhao and P. Lu, *Opt. Express*, 2011, **19**, 4255–4260.

23. Z. Y. Yang, M. Zhao, P. X. Lu and Y. F. Lu, *Opt. Lett.*, 2010, **35**, 2588–2590.

24. J. Kaschke, M. Blome, S. Burger and M. Wegener, *Opt. Express*, 2014, **22**, 19936−19946.

25. M. Esposito, V. Tasco, F. Todisco, M. Cuscunà, A. Benedetti, D. Sanvitto and A. Passaseo, *Nat. Commun*., 2015, **6**, 6484.

26. W. F. van Dorp, C. W. Hagen, *J. Appl. Phys.*, 2008, **104**, 081301.

27. J. M. De Teresa, R. Córdoba, A. Fernández-Pacheco, O. Montero, P. Strichovanec, M.R. Ibarra, *J. Nanomater.* 2009, **2009**, 936863.